POLITECNICO DI TORINO
Repository ISTITUZIONALE

Flux-Map Based FEA Evaluation of Synchronous Machine Efficiency Maps

(Article begins on next page)

07 May 2024

Flux-Map Based FEA Evaluation
of Synchronous Machine Efficiency Maps

Simone Ferrari, *Member, IEEE,* Paolo Ragazzo, *Student Member, IEEE,* Gaetano Dilevrano, *Student Member, IEEE,* and Gianmario Pellegrino, *Senior Member, IEEE*

Department of Energy *Galileo Ferraris*

Politecnico di Torino, Turin, Italy

Emails: simone.ferrari@polito.it, paolo.ragazzo@polito.it, gaetano.dilevrano@polito.it, gianmario.pellegrino@polito.it

Abstract—This paper presents a methodology for the efficiency maps evaluation of synchronous electric machines. The procedure is based on the manipulation of flux maps, iron loss and Permanent Magnet (PM) loss map obtained via 2D Finite Element Analysis (FEA). A step-by-step procedure is given, and made available to engineers in the form of open-source Matlab scripts. Different types of FEA approaches and the effect of the different electric drive control techniques are compared and commented while converging to the proposed method. The methodology is valid for all types of synchronous machines, and finds its prominent field of application in automotive, for electric and hybrid electric traction and on-board generation.

Fig. 1. PM-SyR machine example used throughout the paper. The PMs are dysplayed in blue.

TABLE I
PM-SYR MOTOR RATINGS

Nominal current	i_{nom}	22	[Apk]
Max current	i_{max}	44	[Apk]
Nominal torque	T_{nom}	19	[Nm]
Max torque	T_{max}	43	[Nm]
DC link voltage	V_{dc}	310	[V]
Nominal speed	n_{nom}	2500	[rpm]
Max speed	n_{max}	7000	[rpm]
Nominal power	P_{nom}	5	[kW]
Max power	P_{max}	11.5	[kW]

I. INTRODUCTION

Vector controlled synchronous machines are the state-of-the-art solution for high-efficiency industrial applications and electrified vehicular traction [1] [2].

Synchronous machines can be divided into several categories, mainly depending on the type of rotor excitation. Wound-field synchronous machines are mainly adopted for generation [3] and more rarely in traction. Another kind of synchronous machines are the Synchronous Reluctance (SyR) machines, that are gaining attention for high efficiency industrial applications, but also for traction applications [4], thanks to the simple manufacturing process and the higher efficiency compared to induction motors [5]. Based on the ratio of magnetic to reluctance torque, the vast category of Permanent-Magnet Synchronous Machines (PMSMs) ranges from Surface-mounted PM (SPM) machines [6] [7] to Interior Permanent Magnet (IPM) machines [8], to the PM-assisted Synchronous Reluctance (PM-SyR) machines.

One of the key figures for the electric machine evaluation is the efficiency map, that express the motor efficiency function of torque and speed. Efficiency maps are important for all the applications that require multiple working points on the torque-speed plane, as for traction applications. There motor works in several operating points and motor loss heavily impacts the battery range.

The paper proposes a method to compute the efficiency map of synchronous machines based on the flux maps. These are necessary to account for the strong nonlinear behaviors of most of the synchronous machines. After a brief introduction on the flux maps in Section II, Section III, discusses the accounted losses and the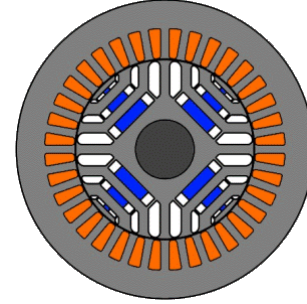 methodologies to compute them through simple 2D FEA simulations. Then, the efficiency map flowchart will be presented and conclusions will be drawn on the results. The procedure is included in SyR-e [9], an open-source framework for electric machines design and evaluation developed in Matlab and linked to the 2D FEA solver FEMM [10]. The benchmark is a PM-SyR machine, first presented in [11], with the main data reported in Table I and the cross-section shown in Fig. 1. Since the computation method is based on flux maps, the proposed procedure is valid for all the machines that can be modeled in this way, and so SyR, IPM and SPM machines. Extensions to wound-field synchronous machines and induction motors can be done under some assumptions and adding some steps to the flowchart.

II. FLUX MAPS COMPUTATION USING FEA SIMULATIONS

Flux maps are obtained using FEA by running several simulations on a regular grid over the (i_d^m, i_q^m) plane. The selection of the FEA simulated points is important, and
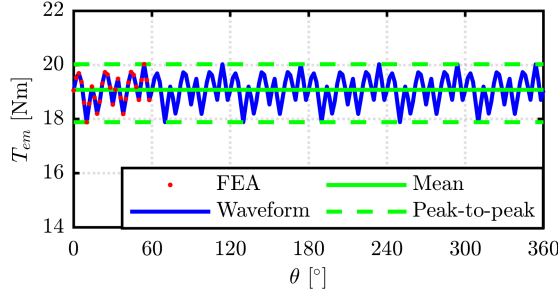
Fig. 2. Torque waveform obtained with 30 rotor positions simulated on 60 electrical degrees: FEA simulations (red dots), complete waveform (blue line), mean torque definition (solid green line) and peak-to-peak torque definition (green dashed lines).
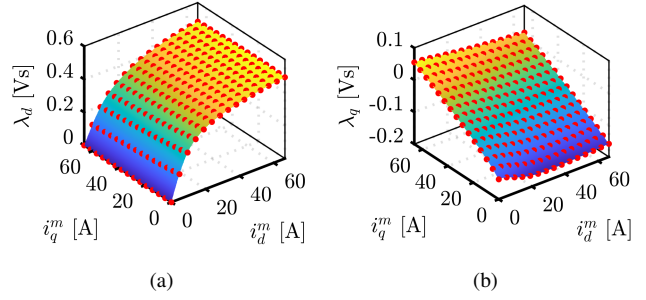

Fig. 3. Flux maps: d-axis flux linkage (a) and q-axis flux linkage (b). Red points represents the FEA simulations, while the surfaces are re-interpolated over a finer grid.

represents a trade-off between accuracy and computational speed. To further speed-up the flux maps evaluation, other techniques can be adopted. They usually target to reduce the computational time of the single (i_d^m, i_q^m) point, and are:

- 2D FEA models instead of 3D FEA. The 3D effects, as end-turns inductance and resistance, can be added later.
- Static models instead of transient models. This simplification stands only for current-supplied model in steady-state condition, which are the conditions of the flux maps computation. The rotor movement is emulated by running several static simulations at different rotor position, representing different time frames.
- Geometric symmetry: instead of simulating the entire motor, just one or two poles can be simulated, exploiting the periodic or anti-periodic symmetry of the motor and reducing the size of the problem.
- Electric symmetry: simulation of a fraction of the electrical period rotation of the rotor ($\frac{1}{6}$ of the electrical period for standard 3-phase distributed winding motors), reducing the total number of simulations [12].

Fig. 2 shows a torque waveform computed with $i_d^m = 16\,\text{A}$ and $i_q^m = 15\,\text{A}$ of the benchmark motor. The red dots denotes the FEA simulations (30 simulations over 60 electrical degrees, in this case), while the blue line represents the complete waveform over one electrical period. From this data, further manipulation gives representative values that can be saved in the flux maps, such as the average value, peak-to-peak ripple, harmonic components and so on. The example shows torque, but the same process can be performed on dq flux linkage components.

A. 2D Maps Organization

The flux maps are organized as 2D matrices, according to the i_d^m, i_q^m grid represented by the matrices $\mathbf{I_d^m}$ (repetition of the i_d^m vector by rows) and $\mathbf{I_q^m}$ (repetition of the i_q^m vector by columns). This matrices will be denoted in the following with capital bold font, as reported for the magnetizing current components, to have a simple and short notation to identify the maps. It must be remarked that the flux maps are reported as a function of the magnetizing component of the current, denoted with the subscript "m", as will be clarified later. For each point of the current grid, a 2D static FEA simulation can

be performed and average dq flux linkage values are saved in the matrices $\mathbf{\Lambda_d}(i_d^m, i_q^m)$ and $\mathbf{\Lambda_q}(i_d^m, i_q^m)$, reported in Fig. 3.

Usually, this data organization can be adopted to store additional data, such as the average electromagnetic torque map $\mathbf{T_{em}}(i_d^m, i_q^m)$, the peak-to-peak torque ripple map $\mathbf{\Delta T_{em}}(i_d^m, i_q^m)$ and so on. Fig. 3 shows the flux maps: FEA results are reported with red dots (a 15x15 grid was simulated) and the maps are interpolated over a finer grid (256x256 points) to ease the further manipulations.

It is important to highlight that the flux maps are function of the PM temperature, and so if the PM temperature changes, the flux map must be re-computed.

The flux maps evaluation is defined as an "embarrassingly parallel problem", since the computation of one current point is independent from the other points. For this reason, parallel computing can be easily adopted to further speed-up the flux maps evaluation. For instance, to obtain the flux maps reported in Fig. 3, a 15x15 grid was simulated, with 30 rotor position on 60 electrical degrees. The flux maps takes less than one hour to be computed, exploiting the parallel computing on a standard laptop, with an Intel i7-8750H CPU (6 cores) and 16 GB RAM.

III. EFFICIENCY MAP COMPUTATION FROM FLUX AND LOSS MAPS

The efficiency versus torque and speed map is the most synthetic expression of the machine performance. Before introducing the evaluation algorithm, the steady-state model and the loss models needed for the efficiency computation are briefly introduced.

A. Steady-State Model of the AC Machine

The steady-state model of the AC synchronous machine is reported in (1) and Fig. 4.

$$v_{dq} = R_s \cdot i_{dq} + j \cdot \omega \cdot \lambda_{dq} \qquad (1)$$

The complex notation is adopted, so $v_{dq} = v_d + j \cdot v_q$ is the dq voltage, $i_{dq} = i_d + j \cdot i_q$ is the dq current, R_s is the phase resistance, ω is the electric pulsation and $\lambda_{dq} = \lambda_d + j \cdot \lambda_q$ is the dq flux linkage. The two flux linkage components are a function of the dq magnetizing current $i_{dq}^m = i_d^m + j \cdot i_q^m$

according to the flux maps $\mathbf{\Lambda_d}$ and $\mathbf{\Lambda_q}$. To account for the iron loss, the R_{Fe} branch is added. This branch drains the equivalent current $i_{dq}^{Fe} = i_d^{Fe} + j \cdot i_q^{Fe}$, so the total dq current is:

$$i_{dq} = i_{dq}^m + i_{dq}^{Fe} \qquad (2)$$

The input power is defined as:

$$P_{elt} = \mathbb{R}\left(\frac{3}{2} \cdot v_{dq} \cdot i_{dq}^*\right) = P_{Cu} + P_{Fe} + T_{em} \cdot \frac{\omega}{p} \qquad (3)$$

where $\mathbb{R}$ denotes the real part of the complex number and the superscript "$*$"denotes the complex conjugate operation. The input electric power is also equal to the sum of copper loss P_{cu}, iron loss P_{Fe} and the product between electromagnetic torque T_{em} and mechanical speed $\frac{\omega}{p}$. Substituting (1) and (2) in (3), it is possible to write all the terms on the right side of the equation, and so:

$$P_{Cu} = \frac{3}{2} \cdot R_s \cdot \left(i_d^2 + i_q^2\right) = \frac{3}{2} \cdot R_s \cdot |i_{dq}|^2 \qquad (4)$$

$$P_{Fe} = \frac{3}{2}\omega\left(\lambda_d i_q^{Fe} + \lambda_q i_d^{Fe}\right) = \mathbb{R}\left[\frac{3}{2} \cdot (j\omega\lambda_{dq}) \cdot \left(i_{dq}^{Fe}\right)^*\right] \qquad (5)$$

$$T_{em} = \frac{3}{2}p \cdot \left(\lambda_d i_q^m - \lambda_q i_d^m\right) \qquad (6)$$

The shaft torque T is then obtained by subtracting the mechanical loss from the electromagnetic torque. Assuming the mechanical loss P_{mech}, it results:

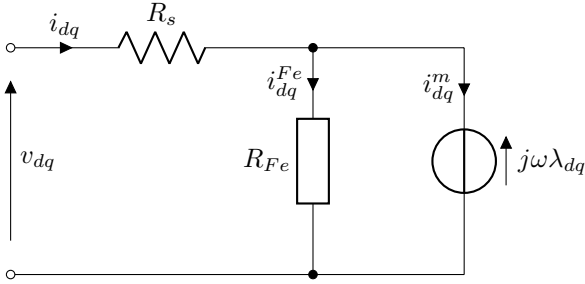$$T = T_{em} - \frac{P_{mech}}{\frac{\omega}{p}} \qquad (7)$$

Fig. 4. Steady state equivalent circuit model of the machine

B. Iron Loss Model

There are several ways to model iron loss. In the following, the modified Steinmetz equation (8) will be adopted. Here, iron loss are divided into two terms: hysteresis loss and eddy-current loss.

$$p_{Fe} = k_h \cdot f^\alpha \cdot B^\beta + k_e \cdot (f \cdot B)^2 \qquad (8)$$

Where B is the flux density in the iron section. The coefficients of the equation can be obtained by fitting the loss data from the manufacturer datasheet. For the benchmark motor, the M330-50A steel grade is adopted, and the coefficients are $k_h = 7.55e^{-3}$, $k_e = 6.36e^{-5}$, $\alpha = 1.30$ and $\beta = 1.80$. Iron losses

are mapped over the (i_d^m, i_q^m) domain, in a similar fashion as the flux maps, at a fixed speed n_0. The results are two maps $\mathbf{P_{h,0}}$ and $\mathbf{P_{e,0}}$, that represents the hysteresis loss and the eddy-current loss respectively, function of i_{dq}^m, for the frequency $f_0 = n_0 \cdot \frac{60}{p}$.

To compute the iron loss maps at different speed (i.e. different frequency), the maps must be rescaled, according to:

$$\mathbf{P_{Fe}} = \mathbf{P_{h,0}} \cdot \left(\frac{f}{f_0}\right)^\alpha + \mathbf{P_{e,0}} \cdot \left(\frac{f}{f_0}\right)^2 \qquad (9)$$

C. Permanent Magnets Loss Model

Permanent magnet loss are caused by the eddy-current circulation in the PM blocks. The proposed procedure adopts a simplified model of the PM loss computation because this loss term in minor compared to the other losses. Furthermore, PMs are usually axially-segmented for manufacturing reason, further reducing the eddy-currents and so the PM loss.

The first assumption made for the PM loss model is to neglect the effect of the eddy currents on the flux distribution. This assumption is in general conservative and is relevant for SPM machines, where the flux linkage relies on PMs, while holds for IPM and PM-SyR machines. The second assumption is to consider PM loss proportional to f^2 as for the eddy-current term of the iron loss. This strongly simplifies the data manipulation, but at the cost of possible overestimation of PM loss. Thanks to these assumptions, PM loss $\mathbf{P_{PM,0}}$ can be computed, as iron loss, over a (i_d^m, i_q^m) grid at fixed speed n_0, and then rescaled as:

$$\mathbf{P_{PM}} = \mathbf{P_{PM,0}} \cdot \left(\frac{f}{f_0}\right)^2 \qquad (10)$$

D. AC Copper Loss Model

Another important loss term is the AC winding loss, caused by skin proximity effects. This is of particular importance for traction motors using hairpin windings of large cross section, rather then wire bundles.

The AC loss factor k_{AC} is defined as the ratio between the copper loss with AC current and the DC loss for the same current (11).

$$k_{AC}(f, \Theta_s) = \frac{P_{Cu,AC}}{P_{Cu,DC}} \qquad (11)$$

Once the slot and conductor geometries are fixed, k_{AC} is function of the fundamental frequency f and the stator temperature Θ_s, that change the resistivity of the material, and hence the magnetic field distribution.

The AC loss factor is computed through simple linear time-harmonic FEA simulations, neglecting the iron saturation. The slot model of the motor under test is reported in Fig. 5. First, the DC copper loss $P_{Cu,DC}$ are computed from FEA model. Then several combination of frequency and temperature are simulated, computing the AC loss $P_{Cu,AC}$, and finally the AC factor, using (11). The results from the benchmark motor are reported in Fig. 5a, where the AC factor is reported as a function of the frequency for some temperatures. As expected, the AC factor is small for the considered PM-SyR motor, since it uses a standard stranded winding.
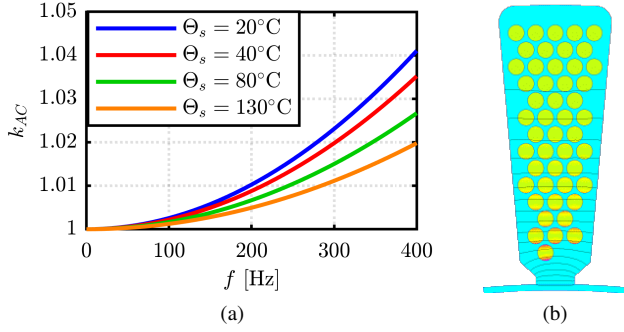
Fig. 5. AC factor function of the frequency, for different winding temperature (a) and slot model solved at 300 Hz and 20°C.

E. Mechanical Loss Model

Mechanical loss are not easy to estimate beforehand, but they can be expressed as a polynomial function of the rotor speed. The literature usually divides mechanical loss into bearing loss, proportional to speed, and windage loss, proportional to the cubic power of the speed. In the following, mechanical loss are modeled with (12), where the factors $a = 0.26$ nW/rpm^3 (bearing loss factor) and $b = 36.5$ mW/rpm (windage loss factor) are fitted from no load test.

$$P_{mech} = a \cdot n^3 + b \cdot n \tag{12}$$

F. Efficiency Maps Computation

The efficiency map is computed on the torque-speed domain. For this reason, new matrices with torque increasing with rows and speed increasing with columns will be adopted and will contains the loss and efficiency data. The evaluation algorithm is organized with two nested for loops: the outer ranging on the speed levels, with index j and the inner ranging on the torque levels, with the index i.

Besides the flux maps and the loss models introduced in the previous sections, the additional data needed for the evaluation are:

- Current and voltage limits I_{max} and V_{max};
- Phase resistance $R_{s,0}$ at reference temperature $\Theta_{s,0}$;
- Target permanent magnet temperature Θ_{PM};
- Target winding temperature Θ_s;
- Control strategy.

About the control strategy, in the following the "maximum efficiency control" will be adopted. It relies on the perfect knowledge of the motor temperature and characteristics; so, it is almost impossible to implement on experimental test-bench, but can give an idea of the best performance of the motor.

It is convenient to define the matrix element-wise product and division, with the symbols "$\odot$"and "$\oslash$"respectively. They will be applied to the flux and loss map matrices (so, matrices function of i_{dq}^m).

The steps of the evaluation procedure are:

1) For a given rotor speed n_j, the electrical frequency f_j and pulsation ω_j are computed.
2) Stator resistance R_s is computed with (13), accounting for the target winding temperature and the AC loss.

$$R_s = k_{AC}(f_j, \Theta_s) \cdot R_{s,0} \cdot [1 + \alpha_s (\Theta_s - \Theta_{s,0})] \tag{13}$$
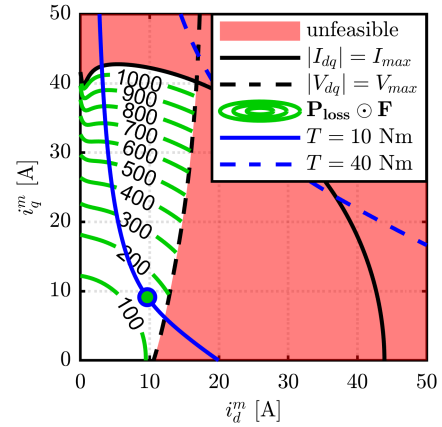

Fig. 6. Graphical explanation of the efficiency map computation on the dq plane at $n_j = 3000$ rpm and $T_i = 40$ Nm (unfeasible point) and $T_i = 10$ Nm (feasible point).

3) Computation of the iron loss map $\mathbf{P_{Fe}}$ and the PM loss map $\mathbf{P_{PM}}$ at the frequency f_j, using (9) and (10).
4) The current representing the iron and PM loss $\mathbf{I_{dq}^{Fe}}$ is computed by inverting (5) for each point of the (i_d^m, i_q^m) map, as:

$$\mathbf{I_{dq}^{Fe}} = \left[\frac{2}{3} \cdot (\mathbf{P_{Fe}} + \mathbf{P_{PM}}) \oslash (j \cdot \omega_j \cdot \mathbf{\Lambda_{dq}}) \right]^* \tag{14}$$

5) The total phase current $\mathbf{I_{dq}}$ is computed as the sum of the magnetizing current $\mathbf{I_{dq}^m}$ and the iron loss current $\mathbf{I_{dq}^{Fe}}$, according to (2). Now, the copper loss $\mathbf{P_{Cu}}$ can be computed with (4).
6) Computation of the phase voltage map $\mathbf{V_{dq}}$ according to (1).
7) Computation of the loss map $\mathbf{P_{loss}}$, as sum of all loss terms:

$$\mathbf{P_{loss}} = \mathbf{P_{Cu}} + \mathbf{P_{Fe}} + \mathbf{P_{PM}} + P_{mech} \tag{15}$$

8) Elimination of all the points in the maps that violate the current and voltage limits. To do so, it is convenient to define a feasibility matrix $\mathbf{F}$ defined as:

$$\begin{cases} \mathbf{F} = NaN & \text{where } |\mathbf{I_{dq}}| > I_{max} \\ \mathbf{F} = NaN & \text{where } |\mathbf{V_{dq}}| > V_{max} \\ \mathbf{F} = 1 & \text{elsewhere} \end{cases} \tag{16}$$

where unfeasible points are denoted with NaN. This feasibility matrix can be multiplied term-by-term to the other matrices to delete the unfeasible points from the maps.

9) Computation of the torque matrix $\mathbf{T}$ from the electromagnetic torque $\mathbf{T_{em}}$ and the mechanical loss, using (7).
10) At this point, the inner loop over the torque reference vector starts.
   a) Computation of the torque contour $T = T_i$ from the $\mathbf{T} \odot \mathbf{F}$ map. The result is the family of current coordinates $(i_d^m, i_q^m)_{T_i}$ corresponding to T_i.

b) From the $(i_d^m, i_q^m)_{T_i}$ family, the maximum efficiency point is extracted.

c) Efficiency is finally computed as:

$$\eta_{ij} = \frac{T_{ij} \cdot \frac{\omega_{ij}}{p}}{T_{ij} \cdot \frac{\omega_{ij}}{p} + P_{loss,ij}} \qquad (17)$$

The process is reported in Fig. 6 for $n_j = 3000$ rpm and two levels of torque (10 and 40 Nm), to better explain the operating point selection. If the point is not feasible ($T_i = 40$ Nm), the family $(i_d^m, i_q^m)_{T_i}$ is empty, so the algorithm set the (T_i, n_j) efficiency point as NaN. Conversely, if $(i_d^m, i_q^m)_{T_i}$ is not empty (e.g. $T_i = 10$ Nm), the loss data corresponding to $(i_d^m, i_q^m)_{T_i}$ are extracted from $\mathbf{P_{loss}} \odot \mathbf{F}$. The i_{dq}^m point with minimum loss value (green dot) will be the key to extract from all the values (voltages, flux linkages, currents, loss terms) related to the (T_i, n_j) point, from the respective maps.

G. Computation of the Iron Loss Model: Static versus Transient FEA

Iron loss are in general computed using transient FEA simulation and commercial tools as Simcenter MagNet [13], but in the previous sections, the iron loss are computed using static FEA simulations [10] and the routines included in SyR-e [9].

The procedure to compute iron loss from static FEA simulation is based on (8). For each mesh element, the flux density waveform is extracted and decomposed along the radial and tangential direction. Then, the two loss terms (hysteresis and eddy-current) can be computed. The latter is simpler and, since it is not a function of the hysteresis cycle, can be computed by applying the second term of (8) at each harmonic component of the flux density spectrum. Conversely, the former term of (8) is based on the hysteresis and needs more attention because of the presence of minor loops. The selected approach is to apply the improved Generalized Steinmetz Equation (iGSE) formulation [14] at the two components of the flux density (radial and tangential) of each mesh element, and then sum all the contributions. The comparison between the iron loss maps computed using static FEA and the maps computed with the transient FEA are presented in Fig. 7 for $n = 3000$ rpm. The figure of merit is the iron loss discrepancy $\mathbf{\Delta P_{Fe}}$, defined in (18).

$$\mathbf{\Delta P_{Fe}} = (\mathbf{P_{Fe}}^{static} - \mathbf{P_{Fe}}^{transient}) \oslash \mathbf{P_{Fe}}^{transient} \qquad (18)$$

The static simulations are optimistic compared to transient FEA, and the maximum discrepancy between the two tools is about 28%. This is a good results, since common correction factor adopted by industry for iron loss computation are around $1.5 \sim 2$ and the static FEA are based on an open-source algorithm while transient FEA are computed with a commercial software that implements proprietary algorithms.

IV. Efficiency Maps Result and Comparison

In the following, the procedure presented in the previous section is adopted to compute the efficiency maps and make some comparisons on the base inputs. Assuming that the current and voltage limits are imposed by the inverter, the
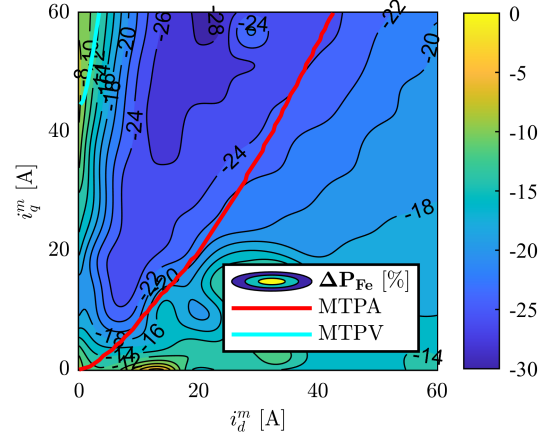

Fig. 7. Discrepancy of the iron loss map computed with static and transient FEA, expressed as percentage of the iron loss map computed with transient FEA.

two parameters that can affect efficiency are temperature and control strategy. The former affects both winding and PMs, increasing stator Joule losses and reducing the PM remanence (and hence, the PMs strength), while the latter is more critical, since the maximum efficiency control is not possible if the motor is not completely identified.

A. Temperature Effects on Efficiency Maps

The first variables taken into account is temperature. Two conditions are considered:

- cold condition: winding temperature $\Theta_s = 40°C$ and PM temperature $\Theta_{PM} = 20°C$;
- hot condition: winding temperature $\Theta_s = 130°C$ and PM temperature $\Theta_{PM} = 120°C$.

The winding temperature affects the stator Joule loss: higher the temperature, higher the phase resistance, and so, higher the loss for the same current. Dealing with the PM temperature, it affects the PM remanence, and, in general, an increase of PM temperature reduces the output torque for a given current. This effect is more evident in the machines with a high PM flux linkage and that use PMs, having a high temperature coefficient.

Fig. 8 compares the efficiency maps in the two thermal conditions. As expected, the efficiency is higher in the cold scenario, thanks to the lower phase resistance and the higher PM remanence. The PM temperature slightly affects also the maximum torque (low speed region): the torque produced in hot condition in slightly lower than the one generated in cold conditions (difference of 1 Nm).

B. Effect of Different Control Strategies

Another important variable that should always be declared with the efficiency map is the control strategy. The procedure presented in the previous section relies on the maximum efficiency control, that ensures the best efficiency that the motor can express, but assumes that the loss maps and the exact temperature of the motor are known a priori. In practice,
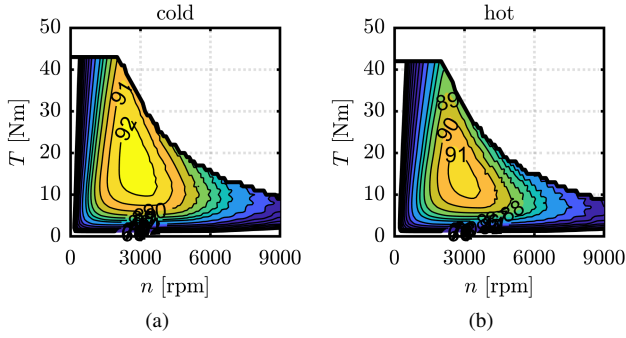
Fig. 8. Efficiency maps of the benchmark motor with maximum efficiency control in cold (a) and hot (b) conditions.
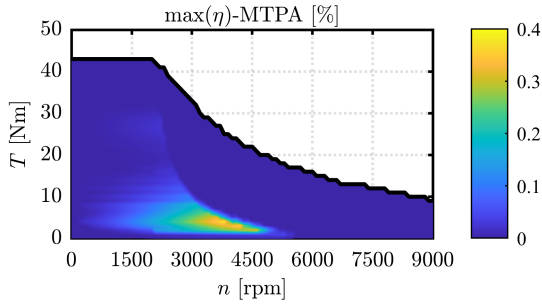

Fig. 9. Difference between the efficiency maps obtained with $max(\eta)$ and MTPA control in cold conditions.

this is not exactly feasible so other controls are implemented. One of the most common control is the Maximum Torque per Ampere (MTPA) control. It consist of minimize the current for a given torque reference and it is based on the simple knowledge of the flux maps (and not the loss maps). At low speed, the MTPA trajectory on the dq plane is followed. Then, as the speed exceeds the base speed, current vector is rotated towards the q axis, until the Maximum Torque per Voltage (MTPV) locus is reached. From this speed on, the current is decreased, according to the MTPV trajectory. The MTPA control can be easily implemented in the efficiency map computation flowchart by using the current map $\mathbf{I_{dq}}$ instead of the loss map $\mathbf{P_{loss}}$ at the step 10-b of the procedure. Maximum efficiency and MTPA control are compared in Fig. 9 that reports the difference in the efficiency obtained with the two methods.

From the analysis it is evident that the difference is in general small and the maximum penalization of the MTPA control (about 0.4% of efficiency) is where iron and PM loss are more important compared to stator Joule loss: for mid-high speed and low torque. Also in the low speed area a small difference is noticeable thanks to the reduction of the iron loss of the maximum efficiency control. Nevertheless, in the high-speed region, the two control strategies are the same, since the voltage and current limits narrow the feasible operating region in the dq plane.

V. CONCLUSION

The paper formalizes the approach of the efficiency map computation of synchronous machines. The process is based on flux maps and relies on FEA simulations performed with open-source FEA tools. Mathematical model of synchronous machine as well as loss model computation are described in order to support the computation algorithm. A PM-SyR motor is adopted as benchmark to support the flowchart explanation and to show the impact of certain inputs on the final results.

The computed efficiency map can be also experimentally validated on a dedicated test-rig, since the dq currents are computed for each working point.

The presented procedure is also included in an open-source framework to the benefit of the academic and industrial community.

REFERENCES

[1] A. Krings and C. Monissen, "Review and trends in electric traction motors for battery electric and hybrid vehicles," in *2020 International Conference on Electrical Machines (ICEM)*, vol. 1, 2020, pp. 1807–1813.

[2] N. Bianchi, S. Bolognani, E. Carraro, M. Castiello, and E. Fornasiero, "Electric vehicle traction based on synchronous reluctance motors," *IEEE Transactions on Industry Applications*, vol. 52, no. 6, pp. 4762–4769, 2016.

[3] Y. Wang, S. Nuzzo, H. Zhang, W. Zhao, C. Gerada, and M. Galea, "Challenges and opportunities for wound field synchronous generators in future more electric aircraft," *IEEE Transactions on Transportation Electrification*, vol. 6, no. 4, pp. 1466–1477, 2020.

[4] J.-R. Riba, C. López-Torres, L. Romeral, and A. Garcia, "Rare-earth-free propulsion motors for electric vehicles: A technology review," *Renewable and Sustainable Energy Reviews*, vol. 57, pp. 367–379, 2016.

[5] R. Leuzzi, P. Cagnetta, S. Ferrari, P. Pescetto, G. Pellegrino, and F. Cupertino, "Transient overload characteristics of pm-assisted synchronous reluctance machines, including sensorless control feasibility," *IEEE Transactions on Industry Applications*, vol. 55, no. 3, pp. 2637–2648, May 2019.

[6] C. He and T. Wu, "Analysis and design of surface permanent magnet synchronous motor and generator," *CES Transactions on Electrical Machines and Systems*, vol. 3, no. 1, pp. 94–100, 2019.

[7] G. Pellegrino, A. Vagati, P. Guglielmi, and B. Boazzo, "Performance comparison between surface-mounted and interior pm motor drives for electric vehicle application," *IEEE Transactions on Industrial Electronics*, vol. 59, no. 2, pp. 803–811, 2012.

[8] Y. Yang, S. M. Castano, R. Yang, M. Kasprzak, B. Bilgin, A. Sathyan, H. Dadkhah, and A. Emadi, "Design and comparison of interior permanent magnet motor topologies for traction applications," *IEEE Transactions on Transportation Electrification*, vol. 3, no. 1, pp. 86–97, March 2017.

[9] F. Cupertino, G. Pellegrino, and et al., "Syr-e: Synchronous reluctance (machines) - evolution," accessed 06-January-2020. [Online]. Available: www.github.com/SyR-e

[10] D. Meeker, "Femm: Finite element method magnetics." [Online]. Available: www.femm.info

[11] S. Ferrari, E. Armando, and G. Pellegrino, "Torque ripple minimization of pm-assisted synchronous reluctance machines via asymmetric rotor poles," in *2019 IEEE Energy Conversion Congress and Exposition (ECCE)*, Sep. 2019, pp. 4895–4902.

[12] G. Y. Sizov, D. M. Ionel, and N. A. O. Demerdash, "Modeling and parametric design of permanent-magnet ac machines using computationally efficient finite-element analysis," *IEEE Transactions on Industrial Electronics*, vol. 59, no. 6, pp. 2403–2413, 2012.

[13] S. I. S. Inc., "Simcenter magnet." [Online]. Available: https://www.plm.automation.siemens.com/global/it/products/simcenter/

[14] K. Venkatachalam, C. R. Sullivan, T. Abdallah, and H. Tacca, "Accurate prediction of ferrite core loss with nonsinusoidal waveforms using only steinmetz parameters," in *2002 IEEE Workshop on Computers in Power Electronics, 2002. Proceedings.*, 2002, pp. 36–41.